Int J Clin Exp Pathol 2026;19(7):304-323
www.ijcep.com /ISSN:1936-2625/IJCEP0171268

Original Article

Single-cell analysis of the synovium and infrapatellar fat pad identifies key pathogenic genes and drug targets in osteoarthritis

Yangming Zhu[2,3*], Yingjia Zhu[4*], Peijian Tong[3], Feng Cheng[1]

[1]Department of Orthopedics, The Third Affiliated Hospital of Zhejiang Chinese Medical University, Hangzhou 310000, Zhejiang, China; [2]The First School of Clinical Medicine, Zhejiang Chinese Medical University, Hangzhou 310000, Zhejiang, China; [3]Institute of Orthopaedics and Traumatology, The First Affiliated Hospital of Zhejiang Chinese Medical University (Zhejiang Provincial Hospital of Chinese Medicine), Hangzhou 310053, Zhejiang, China; [4]Department of Gynecology, Hangzhou Women's Hospital, Hangzhou 310000, Zhejiang, China. [*]Equal contributors and co-first authors.

Received January 5, 2026; Accepted May 18, 2026; Epub July 15, 2026; Published July 30, 2026

Abstract: Objectives: Osteoarthritis (OA) is a chronic degenerative joint disease with great challenges in early diagnosis and treatment, and the synovium and infrapatellar fat pad (IFP) play a synergistic role in its pathological progression. This study aimed to identify OA's key pathogenic cell populations, causal genes, diagnostic biomarkers and potential drug targets from the synovium and IFP via multi-omics analysis and experimental validation, and to evaluate the binding affinity between candidate drug targets and small-molecule compounds by molecular docking, so as to provide new molecular basis and therapeutic strategies for OA. Methods: Single-cell RNA sequencing (scRNA-seq) data of the synovial and IFP tissues (GSE216651) were obtained from the GEO database, and single-cell bioinformatics analyses (clustering, annotation, trajectory and cell-cell interaction analysis) were performed to screen OA-related key cell populations. Two-sample Mendelian randomization (MR) analysis was conducted by integrating OA-GWAS and eQTLGen data to identify OA-causal differentially expressed genes (DEGs), with sensitivity analyses verifying result robustness. PPI network, GO and KEGG analyses were used to elucidate the biological functions of core DEGs. The CeRNA network and DSigDB database were applied to screen diagnostic genes and drug target genes, respectively. An in vitro OA model was established by IL-1α-induced C28/i2 chondrocytes, and qRT-PCR validated the expression of core genes. Virtual screening from FDA database and molecular docking by AutoDock Vina were performed to evaluate the binding affinity of target proteins and candidate compounds. All statistical analyses were conducted with R 4.3, and $P < 0.05$ was statistically significant. Results: Four key OA-associated cell populations (fibroblasts, monocytes, stromal cells, macrophages) were identified, with macrophages specific to the OA group. MR analysis identified 18 OA-causal core DEGs, among which LRRN3 and PTGDS were expressed in the three major cell types. These DEGs were significantly enriched in OA-related processes/pathways such as lipid metabolism and Ras signaling pathway. Four diagnostic genes (GRAMD4, IL15, PITPNM1, SAMD12) and three core drug target genes (SAMD12, PTGDS, INSR) were screened out. qRT-PCR showed INSR was downregulated in the OA model, while the other five core genes were upregulated, consistent with MR results. Molecular docking revealed favorable binding affinity between the three target proteins and FDA-approved compounds; notably, lumacaftor and naldemedine exhibited high binding affinity to two of the three core drug targets, showing multi-target potential for OA treatment. Conclusion: This study identified the key cell populations driving OA progression in the synovium and IFP, and screened four novel diagnostic biomarkers and three potential drug targets for OA, with their expression verified in an in vitro OA model. Lumacaftor and naldemedine were found to have multi-target binding activity to OA core drug targets. These findings deepen the understanding of OA's molecular mechanisms mediated by the synovium and IFP, and provide valuable experimental evidence for OA's early diagnosis and the development of targeted therapeutic drugs, including old drug repurposing.

Keywords: Osteoarthritis, single-cell analysis, Mendelian randomization, pathogenic genes, drug targets

https://doi.org/10.62347/ZICE8570

Introduction

Osteoarthritis (OA) has been identified as a research priority due to its high disability rate and significant impact on the quality of life of patients [1]. Recent studies have demonstrated a strong correlation between the severity of synovial inflammation and the pathogenesis of OA [2]. Notably, synovial inflammation is not only prevalent in OA joints but is also closely associated with imaging diagnosis and pain progression [3]. Synovial inflammation is closely related to clinical manifestations such as knee pain and morning stiffness (less than 30 minutes) [4]; patients with synovitis confirmed by ultrasound or MRI have more significant pain [5]. Consequently, this pathological feature is regarded as a significant early marker of OA development [6]. The infrapatellar fat pad (IFP) has garnered significant attention due to its pivotal role in joint shock absorption and stability maintenance [7]. Growing evidence suggests that the IFP and synovium have a significant synergistic effect in the pathological progression of OA [8]. Specifically, the IFP promotes the progression of OA in collaboration with the synovium through structural remodeling (such as fibrosis and angiogenesis), molecular interactions (such as the regulation of TGFβ and prostaglandin F2α), and immune cell polarization (such as the dynamic changes in macrophage subtypes) [3]. However, despite the increasing number of related studies, further elucidation of the specific molecular mechanisms of the IFP and synovium in OA is required.

Recent technological advances in single-cell analysis have provided a novel approach for the precise diagnosis and treatment of OA, particularly in the analysis of IFP and synovitis cellular heterogeneity, exhibiting unique advantages. Using scRNA-seq technology, researchers have successfully constructed single-cell transcriptomic maps of healthy and OA chondrocytes, revealing significant heterogeneity in chondrocytes [9]. Further single-nucleus RNA sequencing (snRNA-seq) studies found that in OA patients, adipocyte subpopulations (such as ADIPOQ+ cells) and pro-inflammatory fibroblasts in the IFP are significantly expanded, exhibiting gene expression characteristics related to inflammation and extracellular matrix remodeling [10]. In previous studies of synovitis, single-cell analysis revealed the functional heterogeneity of fibroblast-like synoviocytes (FLS). Specific subpopulations (such as PRG4+ and CD55+ FLS) are aberrantly activated in post-traumatic OA, exacerbating synovitis and cartilage degeneration by secreting pro-inflammatory factors (such as IL-6, MMPs) and activating the Wnt/β-catenin signaling pathway [11]. However, traditional omics methods have limitations in elucidating the causal roles of specific cell subpopulations [12]. Therefore, this study introduces Mendelian randomization (MR) analysis to further explore the functional roles of synovial and IFP cell subpopulations in OA progression.

MR is a statistical method that uses genetic variants as instrumental variables (IVs) to infer causal relationships between exposures and outcomes [13]. By integrating pooled data from genome-wide association studies (GWAS), MR can estimate the causal effect of an exposure on an outcome [14, 15]. Furthermore, the integration of MR analysis with GWAS studies has demonstrated a high degree of precision for drug-target confirmation, and MR-validated targets have been shown to exhibit a substantially improved success rate in clinical trials [16]. The use of two-sample MR methods, incorporating GWAS and genetic variants as tools, has yielded substantial evidence for understanding the causes of OA in several studies, and the robustness of the results has been verified by multiple sensitivity analyses, such as MR-Egger, weighted median, etc. [17-19].

This study employed a multi-omics approach by combining GEO gene expression data and genotype-derived expression quantitative trait loci (eQTL) data for MR analysis, revealing key pathogenic genes in the synovium and IFP associated with OA. Subsequent drug prediction and molecular docking validated the pharmacological activity of these potential therapeutic targets, demonstrating their clinical potential.

Materials and methods

The overall study design and technical workflow are illustrated in **Figure 1**, which outlines the strategy for identifying OA pathogenic genes and drug targets from synovial and IFP tissues. First, scRNA-seq data from GEO and GWAS/eQTL data were collected and preprocessed. Next, single-cell analysis (clustering, annota-

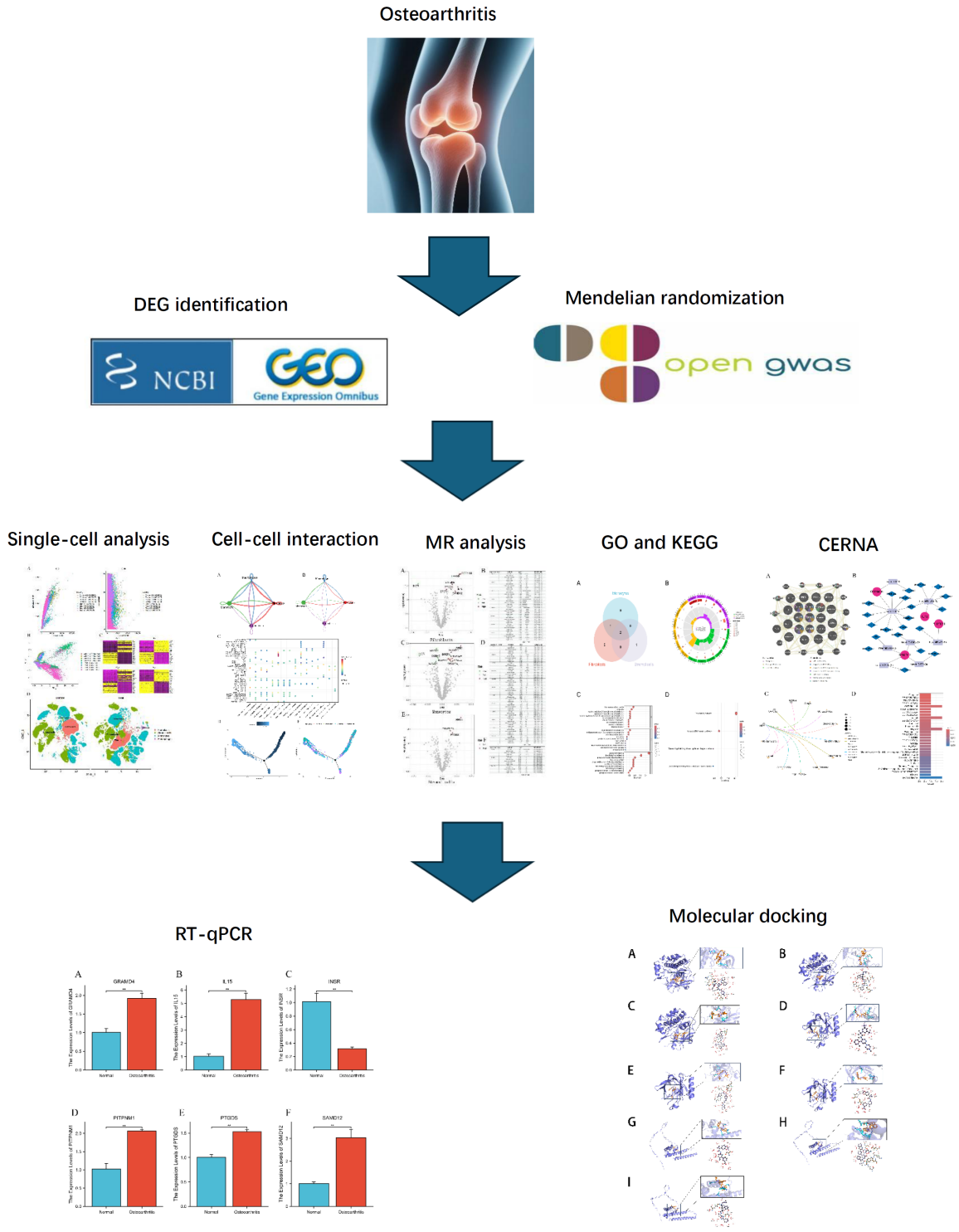

Figure 1. Overview of this study.

tion, trajectory and interaction analysis) was conducted to identify key OA-associated cell populations. Then, MR analysis was used to screen causal DEGs, followed by PPI, GO, KEGG and ceRNA network analyses to determine diagnostic genes and drug target genes. Subsequently, the expression patterns of core genes were validated by qRT-PCR in an IL-1α-

induced OA cell model. Finally, virtual screening from the FDA database and molecular docking were performed to evaluate the binding affinity between candidate drug targets and small-molecule compounds, and to identify potential therapeutic drugs for OA.

Data source

In this study, single-cell RNA sequencing data were obtained from the GEO database of the National Centre for Biotechnology Information (NCBI). The search term "osteoarthritis scRNA-seq" was utilised to identify the relevant dataset, GSE216651. The files matrix.mtx.gz, features.tsv.gz, and barcods.tsv.gz in this dataset, which contain gene expression matrices, gene feature information, and cell barcode information, respectively, were downloaded. The downloaded files were extracted and imported into the R language environment. The data were then pre-processed using the Seurat package, which includes operations such as data quality control, normalization, and dimensionality reduction, to ensure data accuracy and reliability.

From the GWAS database (https://gwas.mrcieu.ac.uk/), we selected outcome data pertaining to OA (ebi-a-GCST90038686), comprising 484,598 samples from Europeans, encompassing data on 9,587,836 SNPs. Data from the eQTLGen consortium (https://www.eqtlgen.org/) were chosen as the exposure, which includes whole blood eQTL data from 31,684 samples, for two-sample MR analysis.

Single-cell sequencing

In the context of single-cell data analysis, the initial step involves the clustering of data, followed by the generation of a cell cluster map by embedding cells in two-dimensional space using the t-SNE algorithm. According to the gene expression characteristics of the cells, the clustered cell populations were annotated to identify different cell types, such as monocytes, fibroblasts, stromal cells, etc. Subsequently, cell trajectory and pseudo-time analysis were conducted using the Monocle3 R package to characterize the dynamic change trajectory of cells during OA pathological progression; the analysis was initiated by normalizing the scRNA-seq expression matrix and defining the cell state with the highly variable genes screened in the clustering step, then ordering the cells along the pseudo-time axis based on gene expression dynamics. The key nodes of cell differentiation and transcriptional changes were identified by detecting the genes with significant expression fluctuations at the branch points of the pseudo-time trajectory, and the expression trends of these marker genes at different pseudo-time stages were visualized to clarify the molecular regulatory characteristics of cell fate transition in OA. Furthermore, cell-cell communication relationships were systematically analysed using the CellChat R package: the gene expression matrix of annotated cell types was imported into the package, and the default human ligand-receptor interaction database was used to calculate the communication probability and interaction strength between different cell pairs. A cell communication network was then constructed with the communication probability as the weight, and the key ligand-receptor pairs of cell-to-cell interactions were screened with the criteria of $P < 0.01$ and communication probability > 0.1, so as to reveal the core signalling mechanism mediating the crosstalk between cells in the OA microenvironment.

Mendelian randomization analysis

To explore the potential causal relationship between genes and OA, this study used MR. First, association analysis was conducted with p1 = 5e-8 and p2 = 5e-8. SNPs with linkage disequilibrium were removed using kb = 10,000 and r2 = 0.001, and weak instrumental variables (F-test value > 10) were excluded. During the two-sample MR analysis, multiple estimation methods were applied, including inverse variance weighting (IVW), weighted median, MR-Egger regression, and simple/weighted mode, to ensure the robustness of the results. inverse variance weighting (IVW) was used as the primary statistical method, with results selected at $P < 0.05$. Additionally, leave-one-out sensitivity analysis and funnel plot were performed to assess the validity of instrumental variables and potential biases.

Bioinformatics

PPI GO KEGG: Based on the key genes identified from the analysis, the GeneMANIA online tool was used to integrate multiple data sources, including physical interactions, co-expres-

sion, prediction, co-localization, and genetic interactions, to construct a protein-protein interaction (PPI) network, revealing the molecular-level interactions of the genes. Additionally, GO functional enrichment analysis and KEGG pathway enrichment analysis were performed on the key genes to understand their enrichment in biological processes, cellular components, and molecular functions, as well as their involvement in signaling pathways. This provides insights into the mechanisms by which genes contribute to the occurrence and progression of OA.

ceRNA network diagram: The competing endogenous RNA (ceRNA) network was constructed in order to reveal the complex interaction among lncRNA, miRNA and mRNA. Firstly, disease-related lncRNA, miRNA and mRNA expression data were obtained from the GEO database. Subsequently, the R software package was employed for data preprocessing, encompassing normalization and differential expression analysis, to identify significantly differentially expressed molecules. Subsequently, potential ceRNA interactions were predicted based on the complementary pairing of miRNAs with lncRNAs and mRNAs. The miRDB database was then utilised to obtain the binding site information of miRNAs and lncRNAs/mRNAs, and the stability of binding was further verified by RNAhybrid and other tools. These interactions were integrated to construct ceRNA networks, which were then visualised using Cytoscape software.

Patent drug gene screening

The relationship files of drugs and genes were obtained from the Drug Signatures Database (DSigDB), and the drugs significantly related to the key genes were identified by enrichment analysis.

Quantitative reverse transcriptase polymerase chain reaction (qRT-PCR)

Human chondrocytes (C28/i2, Reisai, China) were cultured until the 3rd to 5th passage, and then seeded into 6-well plates (5 × 10^5 cells per well). The cells were divided into normal and OA groups. The normal group was treated with high-glucose culture medium without fetal bovine serum, while the OA group was treated with 10 μg/ml of IL-1α. After 24 hours, RNA was extracted from the chondrocytes using the SPARKeasy Cell RNA Rapid Extraction Kit (SparkJade, China). The SPARKscript II RT Plus Kit (with gDNA Eraser) (SparkJade, China) was then employed to remove genomic DNA and reverse transcribe the RNA into cDNA. Finally, qRT-PCR was performed using the ABI7500 fluorescent quantitative PCR instrument (ABI, USA) with the SYBR Green method. After qRT-PCR, the relative expression levels of the target gene were compared to β-actin using the 2-ΔΔCt method. The sequences of primers used for the qRT-PCR assays are listed (Supplementary Table 1). The 20 μL reaction system consisted of 10 μL of 2× SYBR Green Master Mix, 1 μL of cDNA template, 0.4 μL of each primer (10 μM), and 8.2 μL of ddH_2O. The thermal cycling conditions were: 95°C for 30 s, followed by 40 cycles of 95°C for 5 s and 60°C for 30 s. Melting curve analysis was performed at the end of each run to confirm product specificity. Pigds was used as the endogenous reference gene for normalization.

Molecular docking

Target proteins associated with the disease were selected, and their known structures were obtained from the PDB database or predicted using AlphaFold3 for modelling. After optimizing the protein structures by removing water molecules and adding hydrogen atoms using AutoDock software, the structures were saved in .pdbqt format. The mol2 files of 1,615 small-molecule compounds were extracted from the FDA database and converted into .pdbqt format using the MGTools utility. Docking parameters were set (center_x/y/z, size_x/y/z) in AutoDock Vina, and then batch docking was perfomed of the proteins with the small-molecule compounds. The parameters were set as exhaustiveness = 30, num_mode = 9, and energy = 3. After sorting by binding energy, the top three compounds were selected for visual analysis. The 3D conformations were displayed using PyMOL, and 2D interaction diagrams were generated using LigPlus (with blue lines indicating hydrogen bonds and eyelash-like diagrams indicating hydrophobic interactions).

Statistical methods

All statistical analyses were conducted in the R-language (version 4.3), Relative mRNA expression levels were quantified using the 2-ΔΔCt

method and are presented as the mean ± standard deviation (SD) of four independent experiments (n = 4). For comparisons between two groups (Normal vs. OA), Student's t-test was applied. $P < 0.05$ was considered statistically significant. The significance levels for the asterisks used in the figures are defined as follows: *P < 0.05, **P < 0.01, ***P < 0.001.

Results

Single-cell analysis of synovial and infrapatellar fat pads

First, we analyzed the distribution of cell characteristics and the proportion of mitochondrial gene expression in single-cell RNA sequencing (Supplementary Table 2). The first part shows that the total UMI count (nCount_RNA) is positively correlated with the number of genes (nFeature_RNA), with a correlation coefficient of 0.9, indicating a strong correlation between cellular transcriptional activity and mitochondrial gene expression. The second part indicates that the total UMI count is not significantly negatively correlated with the proportion of mitochondrial gene expression (percent.mt) (correlation coefficient of -0.06), suggesting that both data quality and cell type differences are very distinct (**Figure 2A**). Principal component analysis (PCA) was performed on the normal group and OA group to reduce dimensionality and visualize the high-dimensional data, which helped better identify overall expression differences and potential biological variations between the samples. By observing the distribution of samples on PC_1 and PC_2, we eliminated the differences between samples and the effects of treatment on the cellular transcriptome (**Figure 2B**). The heatmap illustrates the relationship between gene expression in single-cell RNA sequencing data and PCA. The figure lists the expression of multiple genes across different principal components (PC_1 to PC_4). The heatmap colours indicate the relative levels of gene expression, helping to identify associations between gene expression patterns and principal components, which allowed us to analyse differences in cell types or states (**Figure 2C**). Finally, we used the t-distributed Stochastic Neighbor Embedding (t-SNE) dimensionality reduction algorithm to show the distribution and types of cells in single-cell RNA sequencing. The axes in the figure represent tSNE_1 and tSNE_2, with different colours and labels representing different cell types, such as monocytes, fibroblasts, stromal cells, and macrophages. By observing the distribution of cells on the 2D plane, we demonstrated the transcriptional heterogeneity and potential intercellular interactions between these four cell types. Complementing our analysis and aiding in the identification of specific cell types. We found that macrophages appeared only in the OA group for OA, which should be closely related to anti-inflammatory effects (**Figure 2D**).

Cell interaction analysis

We first analysed the number of interactions between the four cell types and observed that monocytes and stromal cells had the highest number of interactions (**Figure 3A**). We then analysed the interaction strength among the four types of cells and found that the highest interaction strength was also between monocytes and stromal cells (**Figure 3B**). This indicates that these two types of cells play an important role in cell-to-cell interactions. Through the cell communication bubble chart, we displayed the connections and interactions between the four cell types via ligands and receptors, which play a key role in biological processes such as immune regulation, tissue repair, cell signalling, and metabolic regulation (**Figure 3C**; Supplementary Table 3). Subsequently, we analysed the differentiation or state transition trajectories of the four types of cells using pseudo time analysis of single-cell RNA sequencing data. By projecting cells into a low-dimensional space and ordering them by pseudo time, we revealed the dynamic gene expression patterns and key nodes during cell differentiation or state changes, which helps to understand the mechanisms of cell fate determination (**Figure 3D**). We found that the transformation processes of monocytes, fibroblasts, stromal cells, and macrophages begin with stromal cells differentiating into monocytes at different nodes, and then into macrophages and fibroblasts at different time points in OA (**Figure 3E**).

MR analysis of differential genes in single cells

In order to identify marker genes in each type of cell and genes that have a causal relationship with OA, we conducted MR analysis for screening (Supplementary Table 4). In fibroblasts, 8 differentially expressed genes (DEGs)

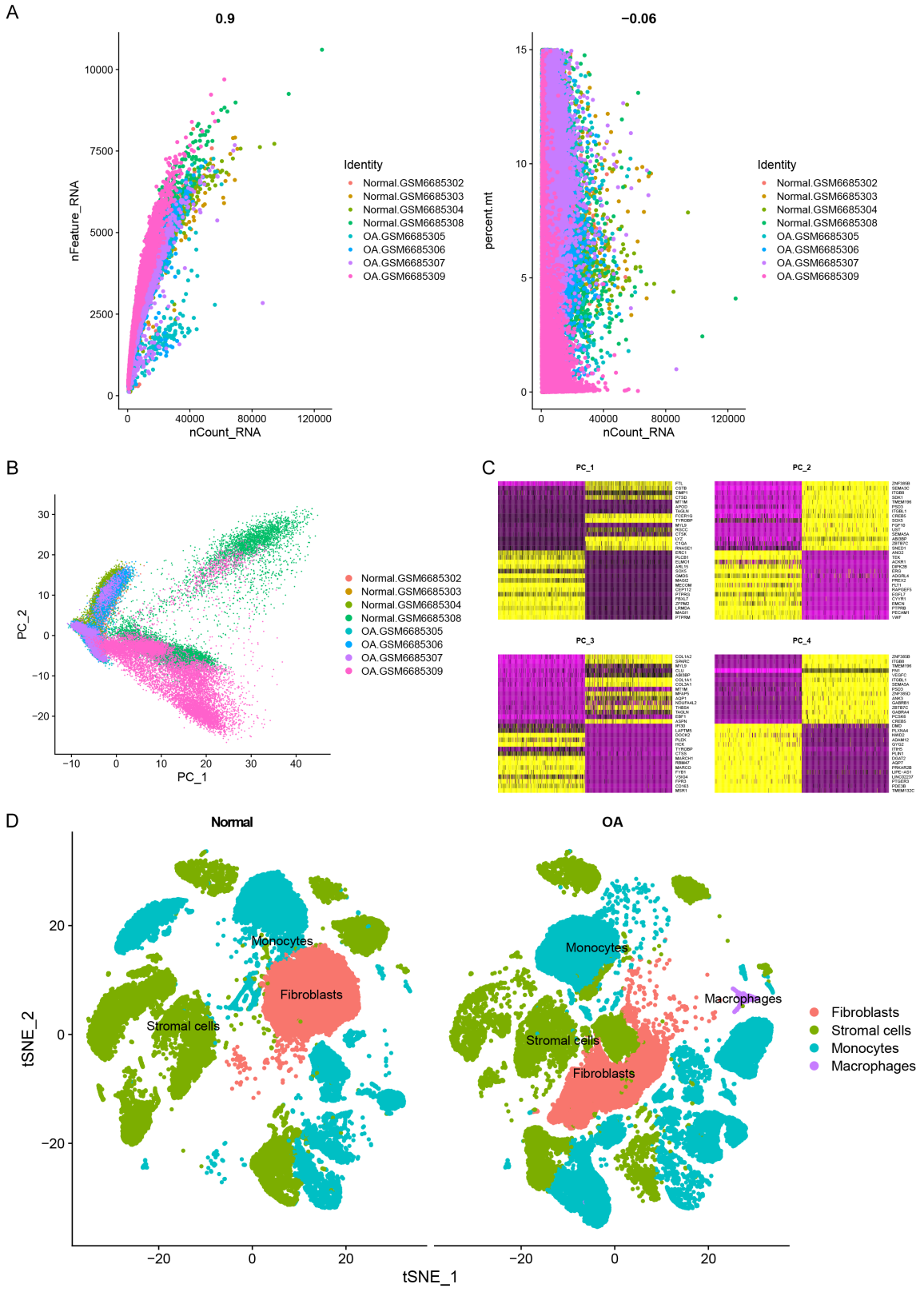

Figure 2. Single-cell analysis of synovium and infrapatellar fat pad. A. Characteristic distribution of cells and mitochondrial gene expression in single-cell RNA sequencing. B. PCA plot of the normal group and OA group. C. Gene expression heatmap from single-cell RNA sequencing data. D. t-SNE plot from single-cell analysis.

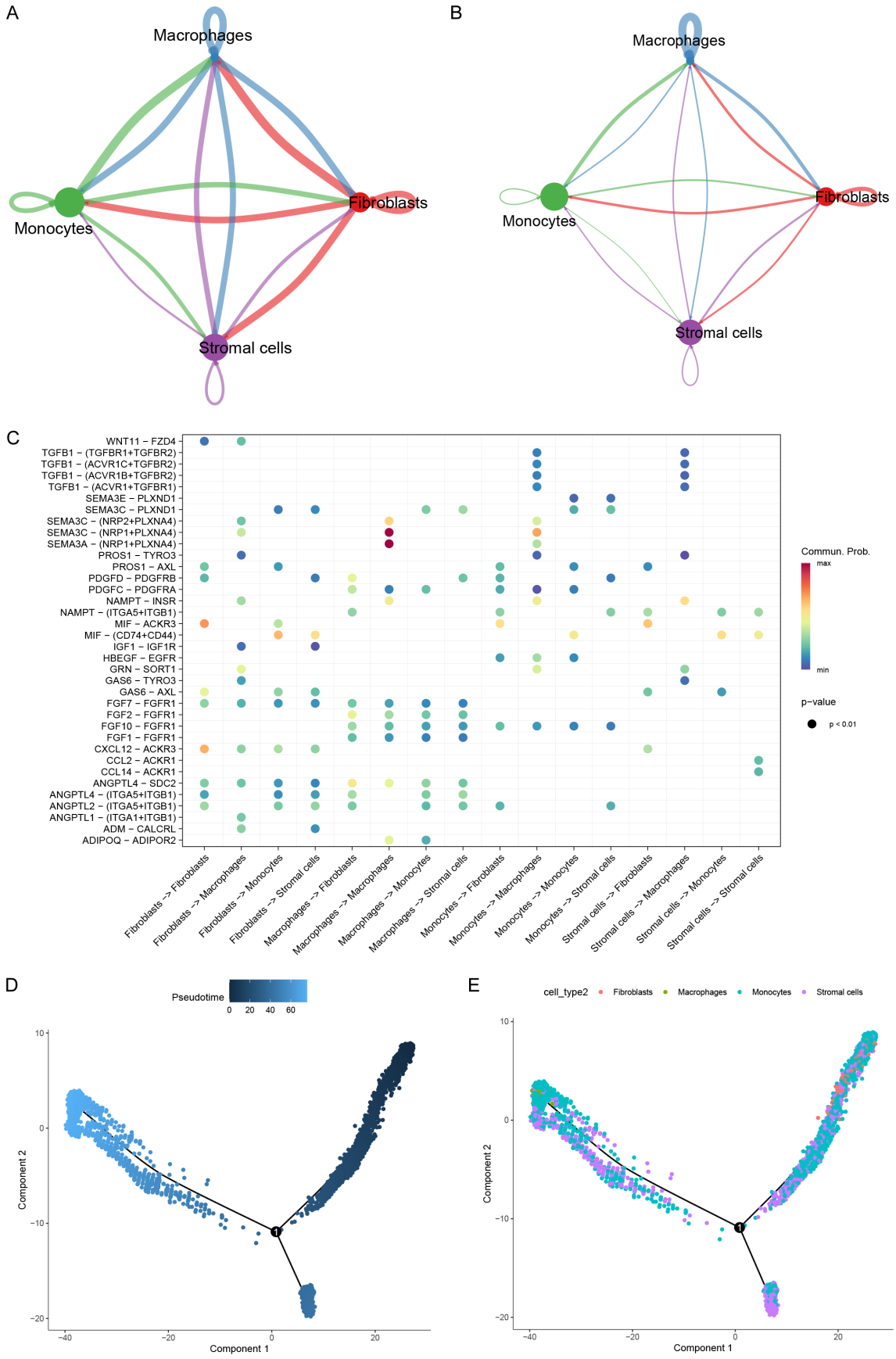
A
Macrophages
Fibroblasts
Monocytes
Stromal cells
B
Macrophages
Fibroblasts
Monocytes
Stromal cells
C
WNT11 – FZD4
TGFB1 – (TGFBR1+TGFBR2)
TGFB1 – (ACVR1C+TGFBR2)
TGFB1 – (ACVR1B+TGFBR2)
TGFB1 – (ACVR1+TGFBR1)
SEMA3E – PLXND1
SEMA3C – PLXND1
SEMA3C – (NRP2+PLXNA4)
SEMA3C – (NRP1+PLXNA4)
SEMA3A – (NRP1+PLXNA4)
PROS1 – TYRO3
PROS1 – AXL
PDGFD – PDGFRB
PDGFC – PDGFRA
NAMPT – INSR
NAMPT – (ITGA5+ITGB1)
MIF – ACKR3
MIF – (CD74+CD44)
IGF1 – IGF1R
HBEGF – EGFR
GRN – SORT1
GAS6 – TYRO3
GAS6 – AXL
FGF7 – FGFR1
FGF2 – FGFR1
FGF10 – FGFR1
FGF1 – FGFR1
CXCL12 – ACKR3
CCL2 – ACKR1
CCL14 – ACKR1
ANGPTL4 – SDC2
ANGPTL4 – (ITGA5+ITGB1)
ANGPTL2 – (ITGA5+ITGB1)
ANGPTL1 – (ITGA1+ITGB1)
ADM – CALCRL
ADIPOQ – ADIPOR2
Fibroblasts –> Fibroblasts
Fibroblasts –> Macrophages
Fibroblasts –> Monocytes
Fibroblasts –> Stromal cells
Macrophages –> Fibroblasts
Macrophages –> Macrophages
Macrophages –> Monocytes
Macrophages –> Stromal cells
Monocytes –> Fibroblasts
Monocytes –> Macrophages
Monocytes –> Monocytes
Monocytes –> Stromal cells
Stromal cells –> Fibroblasts
Stromal cells –> Macrophages
Stromal cells –> Monocytes
Stromal cells –> Stromal cells
Commun. Prob.
max
min
p–value
p < 0.01
D
Pseudotime
0 20 40 60
Component 2
Component 1
E
cell_type2
Fibroblasts
Macrophages
Monocytes
Stromal cells
Component 2
Component 1

Figure 3. Cell interaction analysis of single-cell RNA sequencing data. A. Cell count interaction plot from single-cell RNA sequencing. B. Cell intensity interaction plot from single-cell RNA sequencing. C. Cell communication bubble plot from single-cell RNA sequencing. D. Pseudotime trajectory plot of single-cell RNA sequencing data. E. Cell differentiation trajectory plot from single-cell RNA sequencing data.

were found to have a causal relationship with OA. Among them, 7 genes (EMILIN2, EPDR1, IL15, PITPNM1, SAMD12, LRRN3, and PTGDS) have a detrimental effect on the disease. Which means that the incidence of OA increases with the upregulation of these genes Only INSR has a protective effect, with the incidence of the disease decreasing as its expression level increases (**Figure 4A**, **4B**). In monocytes, 11 genes were found to have a causal relationship with OA. Seven genes (ANKMY1, DPEP2, GRAMD4, LRRN3, IQGAP2, RASA4B, and PTGDS) have a detrimental effect on the disease, while four genes (A4GALT, GSDMB, MYOM1, and INSR) have a protective effect (**Figure 4C**, **4D**). In stromal cells, three genes (LRRN3, PTGDS, and TRAF3IP3) were found to have a causal relationship with OA, and all of them have a detrimental effect on the disease (**Figure 4E**, **4F**).

Bioinformatics analysis of differential genes

The VN plot shows the number and proportion of DEGs in the three types of cells, with a total of 18 DEGs. Among these, LRRN3 and PTGDS are present in all three cell types (**Figure 5A**). Through GO analysis using circle and bubble plots, we identified the functions of these genes, revealing significant enrichment in biological processes such as lipid metabolism, signal transduction regulation, and inflammatory necrosis. Additionally, cellular components such as cytoskeleton structure and membrane contact sites, as well as molecular functions like phosphatidylinositol binding and transfer, also showed significance in the dataset, indicating that these processes and functions play important roles in OA disease (**Figure 5B**, **5C**). In the Kyoto Encyclopedia of Genes and Genomes (KEGG) analysis, the DEGs were significantly enriched in the biosynthesis of glycosphingolipids (lacto and neolacto series, globoseries, and isogloboseries), the cytosolic DNA-sensing pathway, and the Ras signaling pathway. These pathways are involved in key biological processes such as lipid metabolism, immune response, and cellular signaling (**Figure 5D**).

Diagnostic significance of differentially expressed genes and drug target screening analysis

PPI analysis revealed that these DEGs may play important molecular functions in lipid metabolism, signal transduction, and cell membrane structure, which holds significant value in the research of OA disease mechanisms, drug target discovery, and biological process analysis (**Figure 6A**). In the ceRNA network, we identified four genes, GRAMD4, SAMD12, IL15, and PITPNM1, which could serve as diagnostic biomarkers for OA (**Figure 6B**; Supplementary Table 5). Through the gene and drug prediction network, the three genes PTGDS, SAMD12, and INSR interact with multiple drugs, which have potential application value in inflammatory diseases or other metabolic diseases and can be considered as drug targets (**Figure 6C**; Supplementary Table 6). The bar chart of drug-gene interactions illustrates the interactions between drugs and genes. Glargine may interact with INSR to regulate insulin signaling. GSK2220400A, GSK2110236A, GSK1173862A, GSK1326255, and GSK2213727A may interact with PTGDS, SAMD12, or INSR to regulate inflammation, immune response, or metabolic processes. CHROMIUM and retinol may influence gene expression by regulating metabolic processes (**Figure 6D**).

Single-gene MR analysis of core genes

The scatter plots of single genes indicate the causal relationship between each gene and OA. We performed single-gene MR analysis on six genes: GRAMD4, IL15, PITPNM1, PTGDS, SAMD12, and INSR. The results showed that only INSR had a protective effect on OA, while the other five genes had a promoting effect on OA (**Figure 7A-F**). To ensure the reliability of the data, we conducted sensitivity analyses for each gene. All six genes passed the sensitivity tests, indicating the reliability of the data (**Table 1**).

qRT-PCR validation of core genes

In our experimental system, we further validated our findings. The qRT-PCR results indicated

A

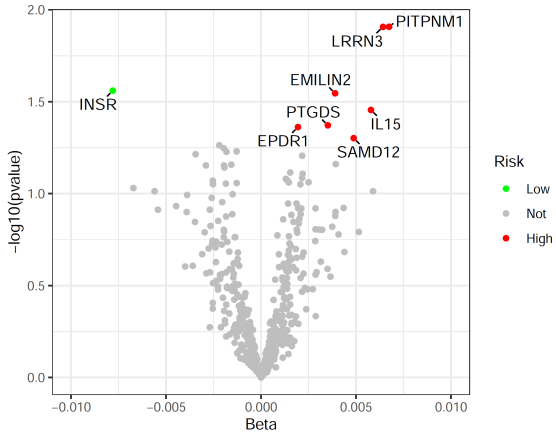

B

exposure	nsnp	method	pval	OR(95% CI)
EMILIN2	5	MR Egger	0.469	1.003 (0.996 to 1.009)
	5	Weighted median	0.077	1.003 (1.000 to 1.007)
	5	Inverse variance weighted	**0.028**	1.004 (1.000 to 1.007)
	5	Simple mode	0.742	1.001 (0.994 to 1.008)
	5	Weighted mode	0.178	1.003 (0.999 to 1.007)
EPDR1	7	MR Egger	0.497	1.002 (0.997 to 1.006)
	7	Weighted median	0.070	1.002 (1.000 to 1.004)
	7	Inverse variance weighted	**0.043**	1.002 (1.000 to 1.004)
	7	Simple mode	0.380	1.003 (0.997 to 1.009)
	7	Weighted mode	0.115	1.002 (1.000 to 1.004)
IL15	4	MR Egger	0.823	1.002 (0.986 to 1.018)
	4	Weighted median	0.079	1.006 (0.999 to 1.012)
	4	Inverse variance weighted	**0.035**	1.006 (1.000 to 1.011)
	4	Simple mode	0.144	1.011 (1.000 to 1.021)
	4	Weighted mode	0.283	1.005 (0.998 to 1.011)
INSR	3	MR Egger	0.616	0.973 (0.900 to 1.052)
	3	Weighted median	0.101	0.993 (0.985 to 1.001)
	3	Inverse variance weighted	**0.028**	0.992 (0.985 to 0.999)
	3	Simple mode	0.327	0.994 (0.984 to 1.003)
	3	Weighted mode	0.326	0.994 (0.984 to 1.003)
LRRN3	5	MR Egger	0.647	1.003 (0.991 to 1.015)
	5	Weighted median	0.072	1.006 (1.000 to 1.012)
	5	Inverse variance weighted	**0.012**	1.006 (1.001 to 1.012)
	5	Simple mode	0.392	1.004 (0.996 to 1.013)
	5	Weighted mode	0.359	1.004 (0.996 to 1.012)
PITPNM1	5	MR Egger	0.626	1.003 (0.993 to 1.012)
	5	Weighted median	0.087	1.005 (0.999 to 1.012)
	5	Inverse variance weighted	**0.012**	1.007 (1.001 to 1.012)
	5	Simple mode	0.253	1.006 (0.997 to 1.015)
	5	Weighted mode	0.212	1.005 (0.998 to 1.012)
PTGDS	3	MR Egger	0.460	1.003 (0.998 to 1.009)
	3	Weighted median	**0.046**	1.003 (1.000 to 1.007)
	3	Inverse variance weighted	**0.043**	1.004 (1.000 to 1.007)
	3	Simple mode	0.438	1.003 (0.997 to 1.009)
	3	Weighted mode	0.217	1.003 (1.000 to 1.007)
SAMD12	4	MR Egger	0.548	1.003 (0.995 to 1.010)
	4	Weighted median	0.057	1.005 (1.000 to 1.011)
	4	Inverse variance weighted	0.050	1.005 (1.000 to 1.010)
	4	Simple mode	0.179	1.007 (0.999 to 1.015)
	4	Weighted mode	0.159	1.005 (1.000 to 1.011)

C

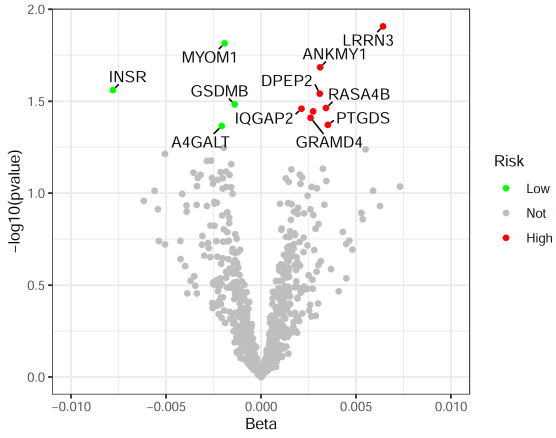

D

exposure	nsnp	method	pval	OR(95% CI)
A4GALT	4	MR Egger	0.321	0.997 (0.993 to 1.001)
	4	Weighted median	**0.043**	0.998 (0.996 to 1.000)
	4	Inverse variance weighted	**0.043**	0.998 (0.996 to 1.000)
	4	Simple mode	0.227	0.997 (0.993 to 1.001)
	4	Weighted mode	0.154	0.998 (0.996 to 1.000)
ANKMY1	3	MR Egger	0.522	1.003 (0.997 to 1.009)
	3	Weighted median	**0.029**	1.003 (1.000 to 1.006)
	3	Inverse variance weighted	**0.021**	1.003 (1.000 to 1.006)
	3	Simple mode	0.217	1.003 (1.000 to 1.007)
	3	Weighted mode	0.199	1.003 (1.000 to 1.006)
DPEP2	7	MR Egger	0.487	1.002 (0.997 to 1.008)
	7	Weighted median	0.069	1.003 (1.000 to 1.006)
	7	Inverse variance weighted	**0.029**	1.003 (1.000 to 1.006)
	7	Simple mode	0.183	1.004 (0.999 to 1.009)
	7	Weighted mode	0.173	1.003 (0.999 to 1.006)
EPHA1−AS1	3	MR Egger	0.927	1.000 (0.993 to 1.008)
	3	Weighted median	**0.035**	1.003 (1.000 to 1.005)
	3	Inverse variance weighted	**0.036**	1.003 (1.000 to 1.005)
	3	Simple mode	0.160	1.004 (1.000 to 1.008)
	3	Weighted mode	0.246	1.002 (0.999 to 1.005)
GRAMD4	3	MR Egger	0.774	1.001 (0.995 to 1.008)
	3	Weighted median	0.050	1.003 (1.000 to 1.005)
	3	Inverse variance weighted	**0.039**	1.003 (1.000 to 1.005)
	3	Simple mode	0.188	1.004 (1.000 to 1.007)
	3	Weighted mode	0.288	1.002 (0.999 to 1.005)
GSDMB	5	MR Egger	0.495	0.999 (0.997 to 1.001)
	5	Weighted median	**0.034**	0.999 (0.997 to 1.000)
	5	Inverse variance weighted	**0.033**	0.999 (0.997 to 1.000)
	5	Simple mode	0.672	1.000 (0.998 to 1.001)
	5	Weighted mode	0.123	0.999 (0.997 to 1.000)
INSR	3	MR Egger	0.616	0.973 (0.900 to 1.052)
	3	Weighted median	0.091	0.993 (0.985 to 1.001)
	3	Inverse variance weighted	**0.028**	0.992 (0.985 to 0.999)
	3	Simple mode	0.314	0.994 (0.984 to 1.003)
	3	Weighted mode	0.351	0.994 (0.983 to 1.004)
IQGAP2	8	MR Egger	0.175	1.002 (0.999 to 1.005)
	8	Weighted median	0.059	1.002 (1.000 to 1.004)
	8	Inverse variance weighted	**0.035**	1.002 (1.000 to 1.004)
	8	Simple mode	0.180	1.003 (0.999 to 1.006)
	8	Weighted mode	0.101	1.002 (1.000 to 1.004)
LRRN3	5	MR Egger	0.647	1.003 (0.991 to 1.015)
	5	Weighted median	0.062	1.006 (1.000 to 1.012)
	5	Inverse variance weighted	**0.012**	1.006 (1.001 to 1.012)
	5	Simple mode	0.369	1.004 (0.996 to 1.013)
	5	Weighted mode	0.361	1.004 (0.996 to 1.012)
MYOM1	6	MR Egger	0.257	0.998 (0.995 to 1.001)
	6	Weighted median	**0.013**	0.998 (0.996 to 1.000)
	6	Inverse variance weighted	**0.015**	0.998 (0.997 to 1.000)
	6	Simple mode	0.134	0.998 (0.995 to 1.000)
	6	Weighted mode	0.059	0.998 (0.996 to 1.000)
PTGDS	3	MR Egger	0.460	1.003 (0.998 to 1.009)
	3	Weighted median	**0.044**	1.003 (1.000 to 1.007)
	3	Inverse variance weighted	**0.043**	1.004 (1.000 to 1.007)
	3	Simple mode	0.437	1.003 (0.997 to 1.009)
	3	Weighted mode	0.193	1.003 (1.000 to 1.007)
RASA4B	4	MR Egger	0.838	1.001 (0.994 to 1.008)
	4	Weighted median	0.062	1.003 (1.000 to 1.007)
	4	Inverse variance weighted	**0.034**	1.003 (1.000 to 1.007)
	4	Simple mode	0.308	1.004 (0.998 to 1.010)
	4	Weighted mode	0.251	1.003 (0.999 to 1.007)

E

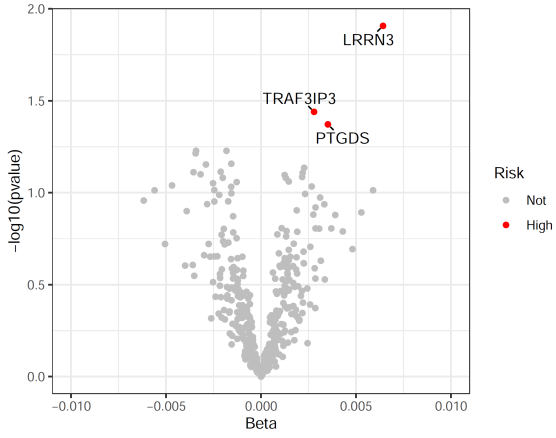

F

exposure	nsnp	method	pval	OR(95% CI)
LRRN3	5	MR Egger	0.647	1.003 (0.991 to 1.015)
	5	Weighted median	0.077	1.006 (0.999 to 1.012)
	5	Inverse variance weighted	**0.012**	1.006 (1.001 to 1.012)
	5	Simple mode	0.350	1.004 (0.996 to 1.012)
	5	Weighted mode	0.364	1.004 (0.996 to 1.012)
PTGDS	3	MR Egger	0.460	1.003 (0.998 to 1.009)
	3	Weighted median	**0.042**	1.003 (1.000 to 1.007)
	3	Inverse variance weighted	**0.043**	1.004 (1.000 to 1.007)
	3	Simple mode	0.455	1.003 (0.997 to 1.009)
	3	Weighted mode	0.187	1.003 (1.000 to 1.007)
TRAF3IP3	3	MR Egger	0.661	1.001 (0.997 to 1.006)
	3	Weighted median	**0.046**	1.003 (1.000 to 1.005)
	3	Inverse variance weighted	**0.036**	1.003 (1.000 to 1.005)
	3	Simple mode	0.297	1.003 (0.999 to 1.007)
	3	Weighted mode	0.226	1.003 (1.000 to 1.006)

Figure 4. MR Analysis of DEGs in single cells. A. Volcano plot of MR analysis of DEGs in fibroblasts. B. Forest plot of MR analysis of DEGs in fibroblasts. C. Volcano plot of MR analysis of DEGs in monocytes. D. Forest plot of MR analysis of DEGs in monocytes. E. Volcano plot of MR analysis of DEGs in stromal cells. F. Forest plot of MR analysis of DEGs in stromal cells.

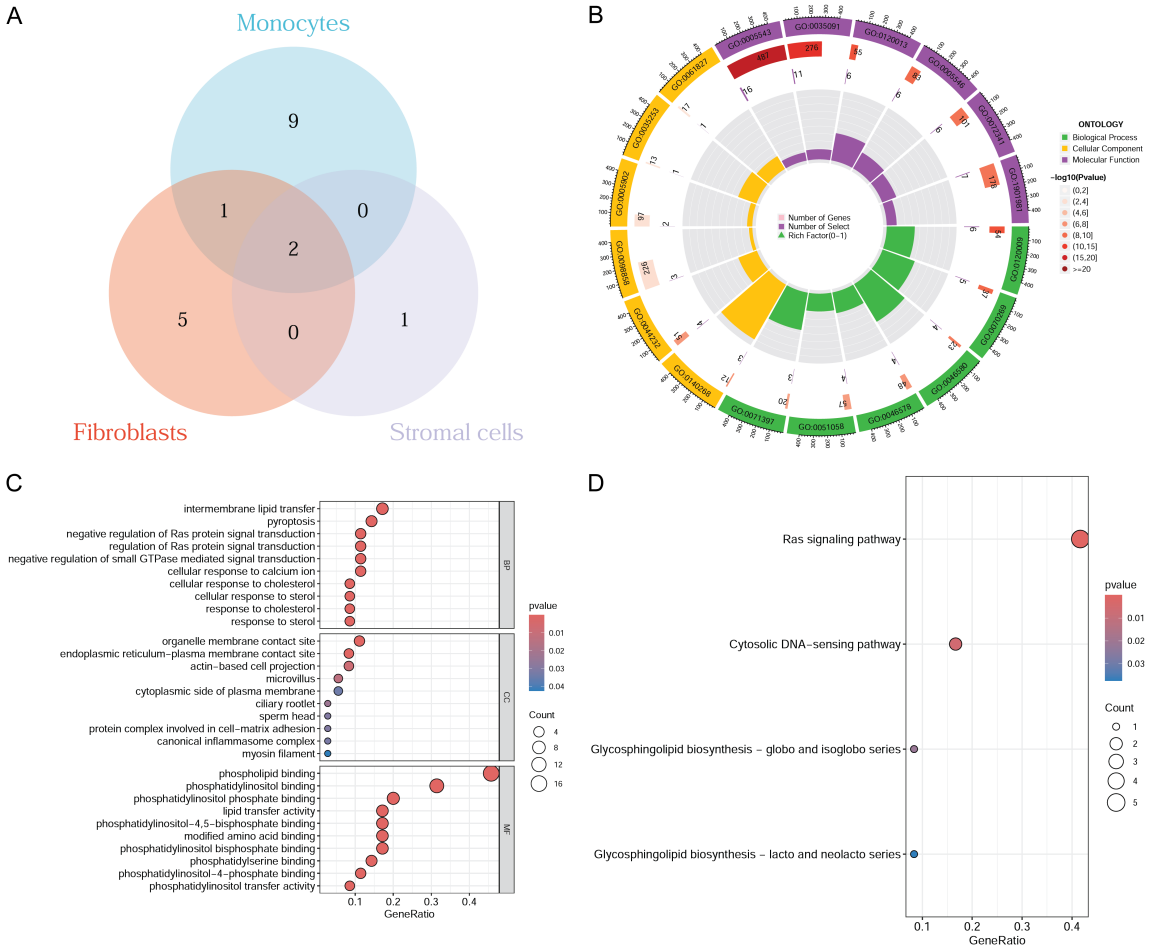

Figure 5. Biological function analysis of DEGs. A. VN plot of DEGs in three cell types. B. Circle plot of GO analysis for DEGs. C. Bubble plot of GO analysis for DEGs. D. Bubble plot of KEGG analysis for DEGs.

the expression differences of the six genes between the normal and OA groups. GRAMD4, IL15, PITPNM1, PTGDS, and SAMD12 showed increased expression in the OA group compared to the normal group, while INSR showed the opposite trend, with decreased expression in the OA group (**Figure 8A-F**). This is consistent with the trend observed through single-gene MR analysis.

Virtual screening and molecular docking analysis

Virtual screening is a key technology in computer-aided drug design, used to screen compound libraries to identify potential drug candidates. The results show that candidate molecules affect DLGAP5 activity through hydrogen bonding (e.g., with residue A) and hydrophobic interactions (e.g., with residue B). The docking results and binding energy data are stored in the designated folder, and the Excel file includes ZINC IDs and SMILES information for traceability. Subsequently, screening of the FDA library identified the top three small molecules with the highest binding scores to INSR: CHEBI:85188, NALEDMEDINE, and Lomitapide, with binding energies of -12.9 kcal/mol, -11.8 kcal/mol, and -11.7 kcal/mol, respectively (**Table 2**; **Figure 9A-C**). The top three small molecules binding to PTGDS were: Netupitant, glimepiride, and Lumacaftor, with binding ener-

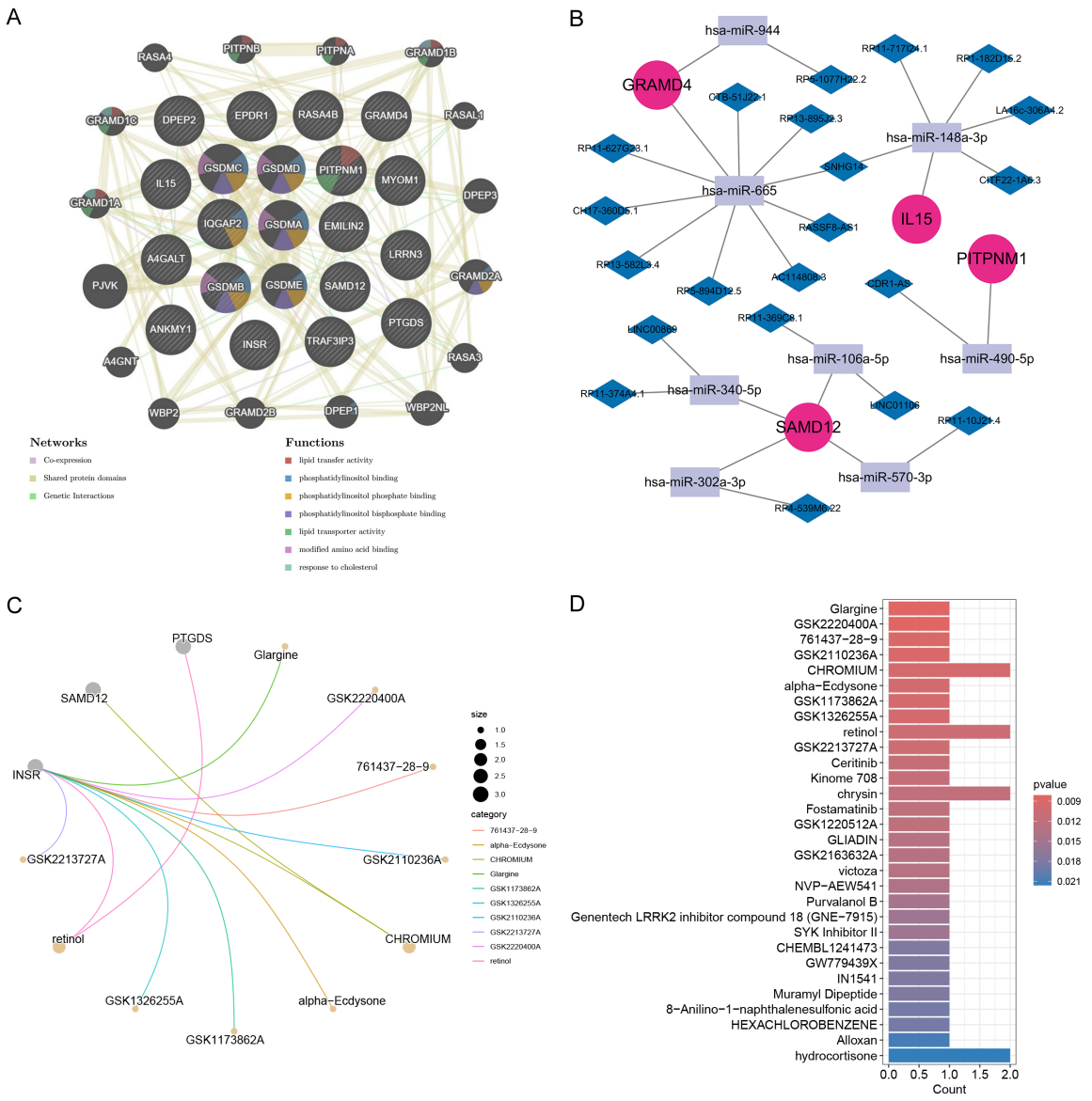

Figure 6. Diagnostic significance of DEGs and drug target screening analysis. A. PPI network of DEGs. B. ceRNA network of core genes. C. Network of drug prediction for core genes. D. Bar chart of drug prediction for core genes.

gies of -11.6 kcal/mol, -11.4 kcal/mol, and -11.2 kcal/mol, respectively (**Table 2**; **Figure 9D-F**). The top three small molecules binding to SMAD12 were: Lumacaftor, SAQUINAVIR, and NALEDMEDINE, with binding energies of -9.6 kcal/mol, -8.9 kcal/mol, and -8.9 kcal/mol, respectively (**Table 2**; **Figure 9G-I**). These findings suggest potential candidates for further research as OA therapeutic agents.

Discussion

This study identified fibroblasts, monocytes, stromal cells, and macrophages as key cell populations in OA through single-cell clustering analysis and cell annotation. Pseudotime analysis of these cell populations showed that, starting from monocytes, stromal cells, and fibroblasts, after passing through the OA node, one branch exhibited a decrease in fibroblasts, while the other branch, based on the reduction of fibroblasts, differentiated into macrophages at the end of the pseudotime sequence. Combined with the results of single-cell analysis, these four types of cells demonstrated a complex interaction network within the tissue microenvironment. The differentiation process of monocytes is subject to regulation by stro-

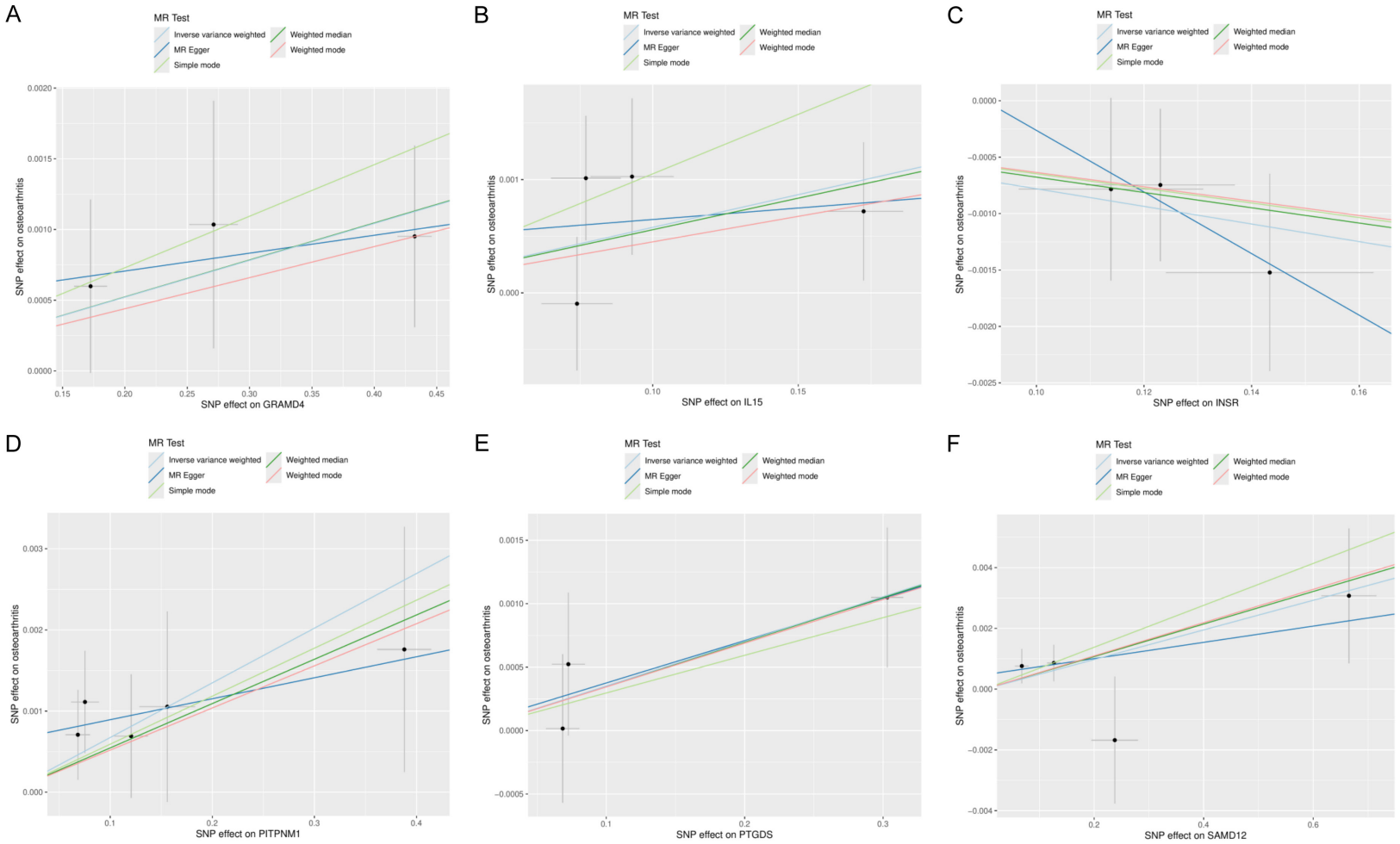

Figure 7. Single-gene MR analysis of core genes. A-F. Scatter plots of MR analysis for six genes: GRAMD4, IL15, PITPNM1, PTGDS, SAMD12, and INSR.

Table 1. Details of the sensitivity analyses for the six core genes

Exposure	Outcome	Heterogeneity tests MR-Egger/IVW Cochran's Q (*P* value)	Directional horizontal pleiotropy test	MR-PRESSO results Global Test/*P* value
GRAMD4	OA	0.094 (0.758)/0.273 (0.872)	0.744	2.854/0.775
IL15	OA	2.263 (0.322)/2.552 (0.465)	0.663	4.420/0.583
INSR	OA	0.084 (0.771)/0.328 (0.848)	0.707	2.144/0.231
PITPNM1	OA	0.354 (0.949)/1.464 (0.832)	0.369	2.604/0.793
PTGDS	OA	0.369 (0.543)/0.374 (0.829)	0.952	2.654/0.787
SAMD12	OA	1.955 (0.376)/2.585 (0.459)	0.510	3.212/0.632

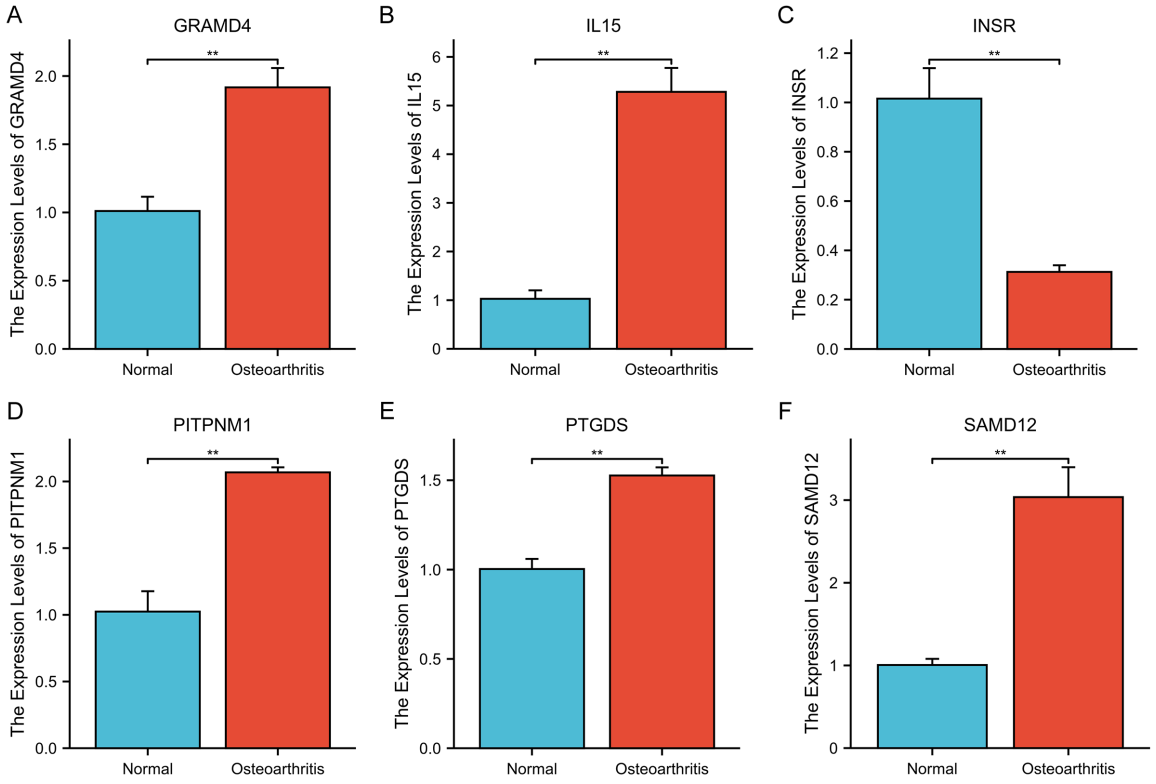

Figure 8. qRT-PCR analysis of the expression differences of six genes between the normal and OA groups. A. GRAMD4 expression was significantly up-regulated in the OA group (1.9-fold of control, P < 0.01). B. IL15 expression was markedly elevated in the OA group (5.0-fold of control, P < 0.01). C. INSR expression was significantly down-regulated in the OA group (0.3-fold INS control, P < 0.01). D. PITPNM1 expression was substantially increased in the OA group (2.1-fold of control, P < 0.01). E. PTGDS expression was notably up-regulated in the OA group (1.5-fold PTG control, P < 0.01). F. SAMD12 expression was significantly elevated in the OA group (3.0-fold xpr control, P < 0.01). Data are expressed as mean ± SD. n = 4 per group. *P < 0.05, **P < 0.01, ***P < 0.001.

mal cells, acting as the precursor cells of macrophages [20]. In OA, articular cartilage fibrosis is one of the key pathological features [21]. Based on the results of single-cell clustering analysis, we hypothesize that there may be a malignant cycle signaling axis in the fibrosis process of OA, composed of monocytes → macrophages → fibroblasts → stromal cells. This axis may promote the pathological progression of OA by regulating cell differentiation and functional states.

The results of single-cell annotation showed that the differentiation of macrophages only occurred in OA samples, which is consistent with previous studies that macrophages have lower activity and number in non-OA samples, and their ability to clear apoptotic cells (effero-

Table 2. Docking results of 3 proteins with small molecules

Target	Structure ID	Drug	PubChem	Binding Energy (kcal/mol)
INSR	5HHW (PDB)	CHEBI:85188	68498031	-12.9
		NALEDMEDINE	54732242	-11.8
		Lomitapide	9853053	-11.7
PTGDS	3O22 (PDB)	Netupitant	6451149	-11.6
		glimepiride	3476	-11.4
		Lumacaftor	16678941	-11.2
SMAD12	Q8N8I0 (AlphaFold)	Lumacaftor	16678941	-9.6
		SAQUINAVIR	441243	-8.9
		NALEDMEDINE	54732242	-8.9

The lower the binding energy, the better the binding effect and the higher the affinity.

cytosis) is not significantly inhibited [22]. Studies have shown that pro-inflammatory M1 macrophages dominate in OA synovium, where they exacerbate cartilage destruction and synovitis through the secretion of inflammatory factors such as IL-1β and TNF-α [23]. Existing research has confirmed that fibroblasts and macrophages are central to the development of fibrosis [24], and intermediate fibroblasts (biglycan-positive) in the OA synovium, together with macrophages, promote fibrosis through APOE signaling [10]. APOE not only directly accelerates the degradation of cartilage proteoglycans but also stimulates fibroblasts to secrete collagen I. these findings are consistent with the results of our cell trajectory analysis: during OA improvement, the number of fibroblasts decreases, while macrophage differentiation significantly increases in the OA progression branch.

Using MR analysis, 18 key core genes were identified. Through KEGG and GO enrichment analyses, we found that these genes were relatively evenly distributed in terms of their impact on biological processes and cellular components, but at the molecular function level, the DEGs were significantly enriched in phospholipid binding functions and highly enriched in the Ras signaling pathway. Previous studies have confirmed that the Ras-related protein Rab-1a affects chondrocyte metabolic homeostasis by regulating autophagy, and that autophagy dysfunction is a key factor in OA cartilage degeneration [25]. In addition, through ceRNA analysis and drug enrichment analysis, we identified four diagnostic marker genes (GRAMD4, IL15, PITPNM1, SMAD12) and three potential drug target genes (SMAD12, PTGDS, INSR) from the DEGs.

PITPNM1, as a membrane-associated phosphatidylinositol transfer protein, mediates the transmembrane transport of phosphatidylinositol and phosphatidic acid through its PITP domain, regulating membrane contact site signaling and lipid homeostasis. Its dysfunction may promote oxidative stress-induced senescence in chondrocytes through the AKT/ERK signaling pathway, thereby driving the progression of OA [26-29].

IL-15 exerts anti-tumor effects in tumor immunity by activating NK cells and CD8+ T cells [30], and is abnormally overexpressed in OA chondrocytes [31]. This suggests that inhibitors targeting IL-15 in cancer, such as siRNA or NIZ985 [32], may also have a role in joint targeting intervention.

GRAMD4, a member of the cholesterol transport protein family, regulates the TAK1-NF-κB/MAPK signaling axis through its GRAM/VASt domain [33-35]. Its dysfunction may participate in the inflammation-metabolism imbalance of OA by mediating cholesterol metabolic reprogramming and epigenetic modifications (such as histone ubiquitination) [36]. These findings reveal new molecular nodes between lipid metabolism, inflammation, and cartilage homeostasis regulation. Future studies need to further dissect the spatiotemporal regulatory network of these nodes, explore collaborative intervention strategies between lipidome reprogramming and inflammation pathways, and develop joint-specific therapeutic approaches based on precise delivery technologies.

INSR, as a core receptor in the insulin signaling pathway, may mediate apoptosis inhibition (Caspase-3/Bcl-2 axis) and obesity-related insulin resistance through Circ-INSR, exacerbating joint inflammation and cartilage metabolic disorders. Targeted intervention of Circ-INSR overexpression or S-nitrosylation regulated by SCAN enzymes may simultaneously improve

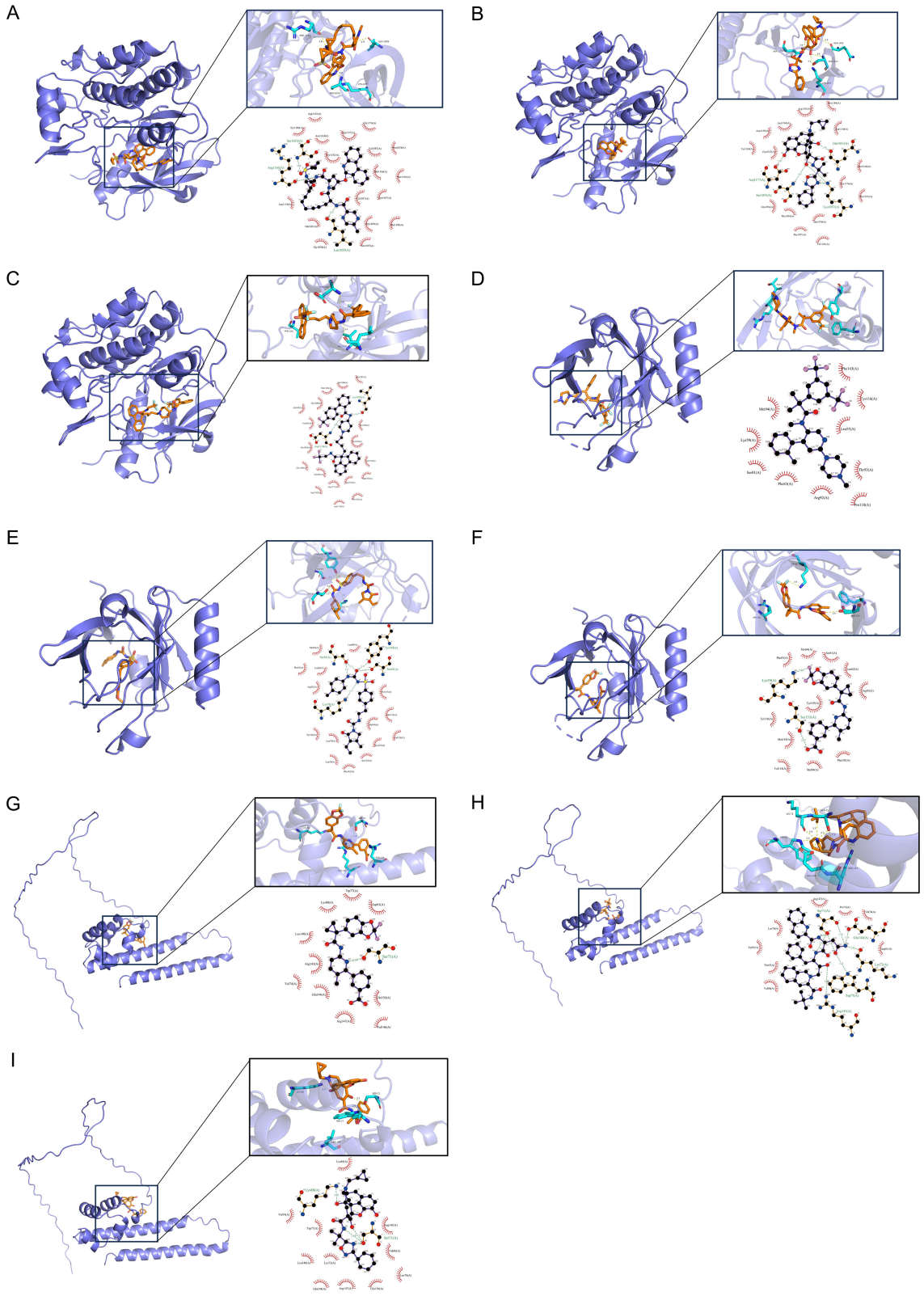

Figure 9. Molecular docking and drug target prediction results. A-C. Molecular docking images and ligand interaction diagrams of INSR with CHEBI:85188, NALEDMEDINE, and Lomitapide. D-F. Molecular docking images and ligand interaction diagrams of PTGDS with Netupitant, glimepiride, and Lumacaftor. G-I. Molecular docking images and ligand interaction diagrams of SMAD12 with Lumacaftor, SAQUINAVIR, and NALEDMEDINE.

metabolism and joint degeneration [27, 37, 38]. PTGDS regulates neuronal sensitization and pain-promoting factors (such as PGE_2) by catalyzing PGD2 production. Inhibition of its activity can induce ferroptosis and delay cartilage degradation. Its inhibitor AT-56 shows synergistic efficacy in pain models and lymphoma, indicating its potential for multi-pathway intervention. Network analysis of drug targets suggests that PTGDS may be a regulatory hub at the intersection of inflammation, cell death, and metabolism pathways [39, 40]. Molecular docking results indicate that CHEBI:85188, Lomitapide, Netupitant, Glimepiride, Lumacaftor, and NALEDMEDINE have high binding scores with the two genes mentioned above. SMAD12, as an inhibitory SMAD, may influence the OA process by regulating chondrocyte differentiation or matrix metabolism. Molecular docking results suggest that SMAD12 has high binding scores with Lumacaftor, SAQUINAVIR, and NALEDMEDINE, indicating its potential as a diagnostic marker or therapeutic target. However, these findings still need further experimental validation.

Non-steroidal anti-inflammatory drugs (NSAIDs), acetaminophen, and intra-articular injection of glucocorticoids or hyaluronic acid remain commonly used first-line or second-line treatment methods in clinical practice. The European Society for the Clinical and Economic Aspects of Osteoporosis, Osteoarthritis and Musculoskeletal Disorders (ESCEO) recommends a multimodal, multi-component and multidisciplinary combined treatment strategy, such as the combination of cartilage protectants (SYSADOAs) with NSAIDs, or the combination of NSAIDs with weak opioids [41]. Some drugs originally used for other diseases have also shown new uses in knee osteoarthritis. For example, oral metformin significantly relieves knee pain in overweight or obese patients with knee osteoarthritis [42]; GLP-1 receptor agonists such as tirzepatide and semaglutide not only lead to significant weight loss but also alleviate pain [43]. Unlike previous studies, the present research identified lumacaftor and naldemedine as multi-target candidate drugs for OA, which have not been reported in previous OA drug repurposing studies. The integrative drug target analysis revealed that Lumacaftor and Naldemedine can exhibit high binding affinity to two key genes. Lumacaftor is currently mainly used to treat patients with cystic fibrosis carrying the F508del-CFTR mutation [44]. Naldemedine, as an oral peripheral μ-opioid receptor antagonist, is primarily used to relieve opioid-induced constipation [45]. In addition, studies have shown that the combination of μ-receptor agonists and δ-receptor antagonists (such as UFP-505) can enhance analgesic effects and reduce the risk of tolerance [46]. This finding suggests that optimizing drug strategies through receptor combinations may provide a new direction for the treatment of OA.

This study has yielded some meaningful results, but there are still some limitations. The heterogeneity of public database data (differences in experimental design, population representativeness bias, and missing non-coding regulatory data) may weaken the credibility of the results. The instrumental variable assumptions in MR analysis are at risk (horizontal pleiotropy interference, insufficiently resolved tissue-specific regulatory mechanisms, and effect estimation bias caused by differences in linkage disequilibrium patterns). The experimental validation system is inadequate (only qRT-PCR validation, limitations of animal models, lack of crystal structure validation and high-throughput screening for drug target prediction). The dropout effect of single-cell data and the *P*-value threshold setting in GWAS analysis may miss biologically meaningful variants. Future research still needs to integrate multi-omics data and conduct multidimensional experimental validation.

Conclusions

We successfully identified and validated several core pathogenic genes and potential drug target genes associated with OA through integrated bioinformatics analyses and experimental validation. These findings provide valuable insights into the molecular mechanisms underlying OA and highlight promising therapeutic targets for the future development of OA-specific drugs.

Acknowledgements

The authors thank all participants in this study. This work was supported by the National Science Foundation of China (82274547) and Administration of Traditional Chinese Medicine of Zhejiang Province, China (2024ZL519).

Disclosure of conflict of interest

None.

Address correspondence to: Feng Cheng, Department of Orthopedics, The Third Affiliated Hospital of Zhejiang Chinese Medical University, Hangzhou 310000, Zhejiang, China. E-mail: chengfeng8302@163.com

References

[1] Osteoarthritis. Nat Rev Dis Primers 2025; 11: 11.

[2] Ebata T, Terkawi MA, Kitahara K, Yokota S, Shiota J, Nishida Y, Matsumae G, Alhasan H, Hamasaki M, Hontani K, Shimizu T, Takahashi D, Endo T, Onodera T, Kadoya K and Iwasaki N. Noncanonical pyroptosis triggered by macrophage-derived extracellular vesicles in chondrocytes leading to cartilage catabolism in osteoarthritis. Arthritis Rheumatol 2023; 75: 1358-1369.

[3] Sanchez-Lopez E, Coras R, Torres A, Lane NE and Guma M. Synovial inflammation in osteoarthritis progression. Nat Rev Rheumatol 2022; 18: 258-275.

[4] Duong V, Oo WM, Ding C, Culvenor AG and Hunter DJ. Evaluation and treatment of knee pain: a review. JAMA 2023; 330: 1568-1580.

[5] McAlindon TE, LaValley MP, Harvey WF, Price LL, Driban JB, Zhang M and Ward RJ. Effect of Intra-articular triamcinolone vs saline on knee cartilage volume and pain in patients with knee osteoarthritis: a randomized clinical trial. JAMA 2017; 317: 1967-1975.

[6] Atukorala I, Kwoh CK, Guermazi A, Roemer FW, Boudreau RM, Hannon MJ and Hunter DJ. Synovitis in knee osteoarthritis: a precursor of disease? Ann Rheum Dis 2016; 75: 390-395.

[7] Jiang LF, Fang JH and Wu LD. Role of infrapatellar fat pad in pathological process of knee osteoarthritis: future applications in treatment. World J Clin Cases 2019; 7: 2134-2142.

[8] Li J, Gui T, Yao L, Guo H, Lin YL, Lu J, Duffy M, Zgonis M, Mauck R, Dyment N, Zhang Y, Scanzello C, Seale P and Qin L. Synovium and infrapatellar fat pad share common mesenchymal progenitors and undergo coordinated changes in osteoarthritis. J Bone Miner Res 2024; 39: 161-176.

[9] Huang C, Zeng B, Zhou B, Chen G, Zhang Q, Hou W, Xiao G, Duan L, Hong N and Jin W. Single-cell transcriptomic analysis of chondrocytes in cartilage and pathogenesis of osteoarthritis. Genes Dis 2024; 12: 101241.

[10] Tang S, Yao L, Ruan J, Kang J, Cao Y, Nie X, Lan W, Zhu Z, Han W, Liu Y, Tian J, Seale P, Qin L and Ding C. Single-cell atlas of human infrapatellar fat pad and synovium implicates APOE signaling in osteoarthritis pathology. Sci Transl Med 2024; 16: eadf4590.

[11] Knights AJ, Farrell EC, Ellis OM, Lammlin L, Junginger LM, Rzeczycki PM, Bergman RF, Pervez R, Cruz M, Knight E, Farmer D, Samani AA, Wu CL, Hankenson KD and Maerz T. Synovial fibroblasts assume distinct functional identities and secrete R-spondin 2 in osteoarthritis. Ann Rheum Dis 2023; 82: 272-282.

[12] Peters H, Potla P, Rockel JS, Tockovska T, Pastrello C, Jurisica I, Delos Santos K, Vohra S, Fine N, Lively S, Perry K, Looby N, Li SH, Chandran V, Hueniken K, Kaur P, Perruccio AV, Mahomed NN, Rampersaud R, Syed K, Gracey E, Krawetz R, Buechler MB, Gandhi R and Kapoor M. Cell and transcriptomic diversity of infrapatellar fat pad during knee osteoarthritis. Ann Rheum Dis 2025; 84: 351-367.

[13] Sanderson E, Glymour MM, Holmes MV, Kang H, Morrison J, Munafò MR, Palmer T, Schooling CM, Wallace C, Zhao Q and Smith GD. Mendelian randomization. Nat Rev Methods Primers 2022; 2: 6.

[14] Holmes MV, Richardson TG, Ference BA, Davies NM and Davey Smith G. Integrating genomics with biomarkers and therapeutic targets to invigorate cardiovascular drug development. Nat Rev Cardiol 2021; 18: 435-453.

[15] Larsson SC, Butterworth AS and Burgess S. Mendelian randomization for cardiovascular diseases: principles and applications. Eur Heart J 2023; 44: 4913-4924.

[16] Razuvayevskaya O, Lopez I, Dunham I and Ochoa D. Genetic factors associated with reasons for clinical trial stoppage. Nat Genet 2024; 56: 1862-1867.

[17] Gu Y, Jin Q, Hu J, Wang X, Yu W, Wang Z, Wang C, Liu Y, Chen Y and Yuan W. Causality of genetically determined metabolites and metabolic pathways on osteoarthritis: a two-sample mendelian randomization study. J Transl Med 2023; 21: 357.

[18] Luo H, Zhu Y, Guo B, Ruan Z, Liu Z, Fan Z and Zhao S. Causal relationships between CD25 on immune cells and hip osteoarthritis. Front Immunol 2023; 14: 1247710.

[19] Zhang J, Li K and Qiu X. Exploring causal correlations between inflammatory cytokines and knee osteoarthritis: a two-sample Mendelian randomization. Front Immunol 2024; 15: 1362012.

[20] Trizzino M, Zucco A, Deliard S, Wang F, Barbieri E, Veglia F, Gabrilovich D and Gardini A. EGR1 is a gatekeeper of inflammatory enhancers in human macrophages. Sci Adv 2021; 7: eaaz8836.

[21] Geng N, Fan M, Kuang B, Zhang F, Xian M, Deng L, Chen C, Pan Y, Chen J, Feng N, Liang L, Ye Y, Liu K, Li X, Du Y and Guo F. 10-hydroxy-2-decenoic acid prevents osteoarthritis by targeting aspartyl β hydroxylase and inhibiting chondrocyte senescence in male mice preclinically. Nat Commun 2024; 15: 7712.

[22] Del Sordo L, Blackler GB, Philpott HT, Riviere J, Gunaratnam L, Heit B and Appleton CT. Impaired efferocytosis by synovial macrophages in patients with knee osteoarthritis. Arthritis Rheumatol 2023; 75: 685-696.

[23] Kou L, Huang H, Tang Y, Sun M, Li Y, Wu J, Zheng S, Zhao X, Chen D, Luo Z, Zhang X, Yao Q and Chen R. Opsonized nanoparticles target and regulate macrophage polarization for osteoarthritis therapy: a trapping strategy. J Control Release 2022; 347: 237-255.

[24] Setten E, Castagna A, Nava-Sedeño JM, Weber J, Carriero R, Reppas A, Volk V, Schmitz J, Gwinner W, Hatzikirou H, Feuerhake F and Locati M. Understanding fibrosis pathogenesis via modeling macrophage-fibroblast interplay in immune-metabolic context. Nat Commun 2022; 13: 6499.

[25] Chen Z, Tang M, Wu Z, Lin Y, Wu C, Huang H, Chen J, Zhu Z, Liu Y, Tang S, Ding C and Han W. Increased Rab1a accelerates osteoarthritis by inhibiting autophagy via activation of the mTORC1-S6K pathway. J Adv Res 2025; 75: 607-619.

[26] Xie J, Lin J, Wei M, Teng Y, He Q, Yang G and Yang X. Sustained Akt signaling in articular chondrocytes causes osteoarthritis via oxidative stress-induced senescence in mice. Bone Res 2019; 7: 23.

[27] Yao Q, Wu X, Tao C, Gong W, Chen M, Qu M, Zhong Y, He T, Chen S and Xiao G. Osteoarthritis: pathogenic signaling pathways and therapeutic targets. Signal Transduct Target Ther 2023; 8: 56.

[28] Polianskyte-Prause Z, Arora A, Taskinen JH, Chaurasiya V, Keskitalo S, Tuhkala A, Hilska I, Varjosalo M and Olkkonen VM. The role of Nir2, a lipid-transfer protein, in regulating endothelial cell functions. Biochim Biophys Acta Mol Cell Res 2025; 1872: 119926.

[29] Xu T, Zhai X, Wang R, Wu X, Zhou Z, Shang M, Wang C, Qi T and Yang W. Phosphatidylinositol promoted the proliferation and invasion of pituitary adenoma cells by regulating POU1F1 expression. Cancer Metab 2025; 13: 1.

[30] Mao Y, van Hoef V, Zhang X, Wennerberg E, Lorent J, Witt K, Masvidal L, Liang S, Murray S, Larsson O, Kiessling R and Lundqvist A. IL-15 activates mTOR and primes stress-activated gene expression leading to prolonged antitumor capacity of NK cells. Blood 2016; 128: 1475-1489.

[31] Rice SJ, Beier F, Young DA and Loughlin J. Interplay between genetics and epigenetics in osteoarthritis. Nat Rev Rheumatol 2020; 16: 268-281.

[32] Leidner R, Conlon K, McNeel DG, Wang-Gillam A, Gupta S, Wesolowski R, Chaudhari M, Hassounah N, Lee JB, Ho Lee L, O'Keeffe JA, Lewis N, Pavlakis GN and Thompson JA. First-in-human phase I/Ib study of NIZ985, a recombinant heterodimer of IL-15 and IL-15Rα, as a single agent and in combination with spartalizumab in patients with advanced and metastatic solid tumors. J Immunother Cancer 2023; 11: e007725.

[33] Ge QY, Chen J, Li GX, Tan XL, Song J, Ning D, Mo J, Du PC, Liu QM, Liang HF, Ding ZY, Zhang XW and Zhang BX. GRAMD4 inhibits tumour metastasis by recruiting the E3 ligase ITCH to target TAK1 for degradation in hepatocellular carcinoma. Clin Transl Med 2021; 11: e635.

[34] Xu K, He Y, Moqbel SAA, Zhou X, Wu L and Bao J. SIRT3 ameliorates osteoarthritis via regulating chondrocyte autophagy and apoptosis through the PI3K/Akt/mTOR pathway. Int J Biol Macromol 2021; 175: 351-360.

[35] Ng MYW, Charsou C, Lapao A, Singh S, Trachsel-Moncho L, Schultz SW, Nakken S, Munson MJ and Simonsen A. The cholesterol transport protein GRAMD1C regulates autophagy initiation and mitochondrial bioenergetics. Nat Commun 2022; 13: 6283.

[36] Grandi FC and Bhutani N. Epigenetic therapies for osteoarthritis. Trends Pharmacol Sci 2020; 41: 557-569.

[37] Ansarullah, Jain C, Far FF, Homberg S, Wißmiller K, von Hahn FG, Raducanu A, Schirge S, Sterr M, Bilekova S, Siehler J, Wiener J, Oppenländer L, Morshedi A, Bastidas-Ponce A, Collden G, Irmler M, Beckers J, Feuchtinger A, Grzybek M, Ahlbrecht C, Feederle R, Plettenburg O, Müller TD, Meier M, Tschöp MH, Coskun Ü and Lickert H. Inceptor counteracts insulin signalling in β-cells to control glycaemia. Nature 2021; 590: 326-331.

[38] Lu D, Chatterjee S, Xiao K, Riedel I, Huang CK, Costa A, Cushman S, Neufeldt D, Rode L, Schmidt A, Juchem M, Leonardy J, Büchler G, Blume J, Gern OL, Kalinke U, Wen Tan WL, Foo R, Vink A, van Laake LW, van der Meer P, Bär C and Thum T. A circular RNA derived from the insulin receptor locus protects against doxorubicin-induced cardiotoxicity. Eur Heart J 2022; 43: 4496-4511.

[39] Hu S, Ren S, Cai Y, Liu J, Han Y, Zhao Y, Yang J, Zhou X and Wang X. Glycoprotein PTGDS promotes tumorigenesis of diffuse large B-cell lymphoma by MYH9-mediated regulation of Wnt-β-catenin-STAT3 signaling. Cell Death Differ 2022; 29: 642-656.

[40] Tavares-Ferreira D, Ray PR, Sankaranarayanan I, Mejia GL, Wangzhou A, Shiers S, Uttarkar R, Megat S, Barragan-Iglesias P, Dussor G, Akopian AN and Price TJ. Sex differences in nociceptor translatomes contribute to divergent prostaglandin signaling in male and female mice. Biol Psychiatry 2022; 91: 129-140.

[41] Veronese N, Cooper C, Bruyère O, Al-Daghri NM, Branco J, Cavalier E, Cheleschi S, da Silva Rosa MC, Conaghan PG, Dennison EM, de Wit M, Fioravanti A, Fuggle NR, Haugen IK, Herrero-Beaumont G, Honvo G, Laslop A, Matijevic R, Migliore A, Mobasheri A, Pelletier JP, Prieto Yerro MC, Radermecker RP, Rannou F, Rizzoli R and Reginster JY. Multimodal multidisciplinary management of patients with moderate to severe pain in knee osteoarthritis: a need to meet patient expectations. Drugs 2022; 82: 1347-1355.

[42] Pan F, Wang Y, Lim YZ, Urquhart DM, Estee MM, Wluka AE, Wolfe R and Cicuttini FM. Metformin for knee osteoarthritis in patients with overweight or obesity: a randomized clinical trial. JAMA 2025; 333: 1804-1812.

[43] Betensky DJ, Smith KC, Katz JN, Yang C, Hunter DJ, Collins JE, Feldman CH, Messier SP, Kim JS, Selzer F, Paltiel AD and Losina E. The cost-effectiveness of semaglutide and tirzepatide for patients with knee osteoarthritis and obesity. Ann Intern Med 2025; 178: 1549-1560.

[44] Elborn JS, Ramsey BW, Boyle MP, Konstan MW, Huang X, Marigowda G, Waltz D and Wainwright CE; VX-809 TRAFFIC and TRANSPORT study groups. Efficacy and safety of lumacaftor/ivacaftor combination therapy in patients with cystic fibrosis homozygous for Phe-508del CFTR by pulmonary function subgroup: a pooled analysis. Lancet Respir Med 2016; 4: 617-626.

[45] Markham A. Naldemedine: first global approval. Drugs 2017; 77: 923-927.

[46] Dietis N, Niwa H, Tose R, McDonald J, Ruggieri V, Filaferro M, Vitale G, Micheli L, Ghelardini C, Salvadori S, Calo G, Guerrini R, Rowbotham DJ and Lambert DG. In vitro and in vivo characterization of the bifunctional μ and δ opioid receptor ligand UFP-505. Br J Pharmacol 2018; 175: 2881-2896.